RSS Tech. Report 121599B-1 **Revised: November 3, 2000**

Algorithm Theoretical Basis Document (ATBD)

AMSR Level 2A Algorithm

Peter Ashcroft and Frank J. Wentz

Prepared for:
EOS Project
Goddard Space Flight Center
National Aeronautics and Space Administration
Greenbelt MD 20771

Prepared by:

Remote Sensing Systems
438 First Street, Suite 200, Santa Rosa, CA 95401 (707) 545-2904

Table of Contents

1. Overview and Background Information

1.1 Introduction

Due to diffraction, radiometers of differing frequencies using a common antenna do not generally produce equivalent gain patterns on the Earth surface. Consequently, direct comparison of such observations is complicated by the fact that the measurements do not describe identical locations. The Level 2A algorithm will alleviate this problem by producing several spatially consistent data sets, corresponding to the footprint sizes of the 6.9, 10.7, 18.7, 36.5, and 89 GHz observations. These five sets of antenna patterns are subsequently referred to as resolutions 1 though 5 of the Level 2A data set, corresponding to footprint sizes of approximately 58, 37, 21, 11, and 5 km respectively. Observations will be produced at spatial intervals of approximately 10 km for the next four lowest resolution data sets, and 5 km for the highest resolution set.

Throughout the remainder of this document, brightness temperature measurements derived directly from the Level 1A stage of processing will be referred to as "actual observations." Those brightness temperatures that are the result of a linear combination of actual observations will be identified as "constructed observations," or "effective observations." The gain patterns of the effective observations closely match actual antenna gain patterns while reducing the effect of measurement noise through averaging. For each Level 2A observation within a single scan of the instrument, a set of coefficients describes the relative weights of the neighboring actual observations that are combined to produce the effective observation. These sets of coefficients are unique for every position along the instrument scan, but do not vary from scan to scan.

1.2 Algorithm Description

The technique used to produce the weighting coefficients is known as the Backus-Gilbert method. This technique, originally developed in the context of inversion of seismic signals propagated through the Earth, approximates a given function as a linear superposition of other functions. One of the most significant obstacles to implementation of the Backus-Gilbert method is that calculation of weighting coefficients requires calculation and inversion of large matrices, and is consequently time consuming. This problem is alleviated in computing the Level 2A data set because the antenna patterns and the relative geometry of the observations are known *a priori*. The weighting coefficients can therefore be calculated before observations are actually collected, leaving only the less time consuming task of applying the weighting coefficients when the data is collected.

1.3 Historical Perspective

The idea of applying the Backus-Gilbert method to the microwave radiometer deconvolution problem was first suggested by *Stogryn* [1978]. The technique has subsequently been used by a number of investigators for construction of antenna patterns [*Poe*, 1990; *Robinson et al.*, 1992]. For example, Farrar et al. discuss the effect of

deconvolution on rain rate retrieval algorithms [*Farrar et al.*, 1994]. While much of this work has focused on deconvolution or spatial resolution enhancement, the technique is equally applicable to spatial averaging applications as was pointed out by Poe. As explained more fully below, spatial averaging permits noise reduction that would not be possible for resolution enhancement.

1.4 Instrument Description

The AMSR-E instrument is similar to SSM/I. The major differences are that AMSR has more channels and a larger parabolic reflector. AMSR takes dual polarization observations (v-pol and h-pol) at the 6 frequencies shown in Table 1. The offset 1.6-m diameter parabolic reflector focuses the Earth radiation into an array of 6 feedhorns. The radiation collected by the feedhorns is then amplified by 14 separate total-power radiometers. The 18.7 and 23.8 GHz receivers share a feedhorn, while dedicated feedhorns are provided for the other frequencies. Two feedhorns are required for the 89 GHz channels to achieve 5-km along-track spacing. Figure 1 shows the block diagram for this configuration.

Table 1. Instrument Specifications for AMSR-E

Center Frequencies (GHz)	6.925	10.65	18.7	23.8	36.5	89.0
Bandwidth (MHz)	350	100	200	400	1000	3000
Sensitivity (K)	0.3	0.6	0.6	0.6	0.6	1.1
IFOV (km x km)	75×43	51×29	27×16	32×18	14×8	7×4
Sampling Rate (km x km)	10×10	10×10	10×10	10×10	10×10	5×5
Integration Time (msec)	2.6	2.6	2.6	2.6	2.6	1.3
Main Beam Efficiency (%)	95.3	95.0	96.3	96.4	95.3	96.0
Beamwidth (degrees)	2.2	1.4	0.8	0.9	0.4	0.18

The parabolic reflector and feedhorn array are mounted on a drum containing the radiometers, digital data subsystem, mechanical scanning subsystem, and power subsystem. The reflector/feed/drum assembly is rotated about the axis of the drum by a coaxially mounted bearing and power transfer assembly. All data, commands, timing and telemetry signals, and power pass through the assembly on slip ring connectors to the rotating assembly.

A cold reflector and a warm load are mounted on the transfer assembly shaft and do not rotate with the drum assembly. They are positioned off axis such that they pass between the feedhorn array and the parabolic reflector, occulting it once each scan. The cold reflector reflects cold sky radiation into the feedhorn array thus serving, along with the warm load, as calibration references for the AMSR.

The AMSR rotates continuously about an axis parallel to the spacecraft nadir at 40

rpm. At an altitude of 705 km, it measures the upwelling Earth brightness temperatures over an angular sector of ± 90° degrees about the sub-satellite track, resulting in a swath width of 1670 km. During a scan period of 1.5 seconds, the spacecraft sub-satellite point travels 10 km. Even though the instantaneous field-of-view for each channel is different, Earth observations are recorded at equal intervals of 10 km (5 km for the 89 GHz channels) along the scan. The two 89-GHz feedhorns are offset such that their two scan lines are separated by 5 km in the along-track direction. The nadir angle for the parabolic reflector is fixed at 47.4°, which results in an Earth incidence angle θ_i of 55° ± 0.3°. The small variation in θ_i is due to the slight eccentricity of the orbit and the oblateness of the Earth.

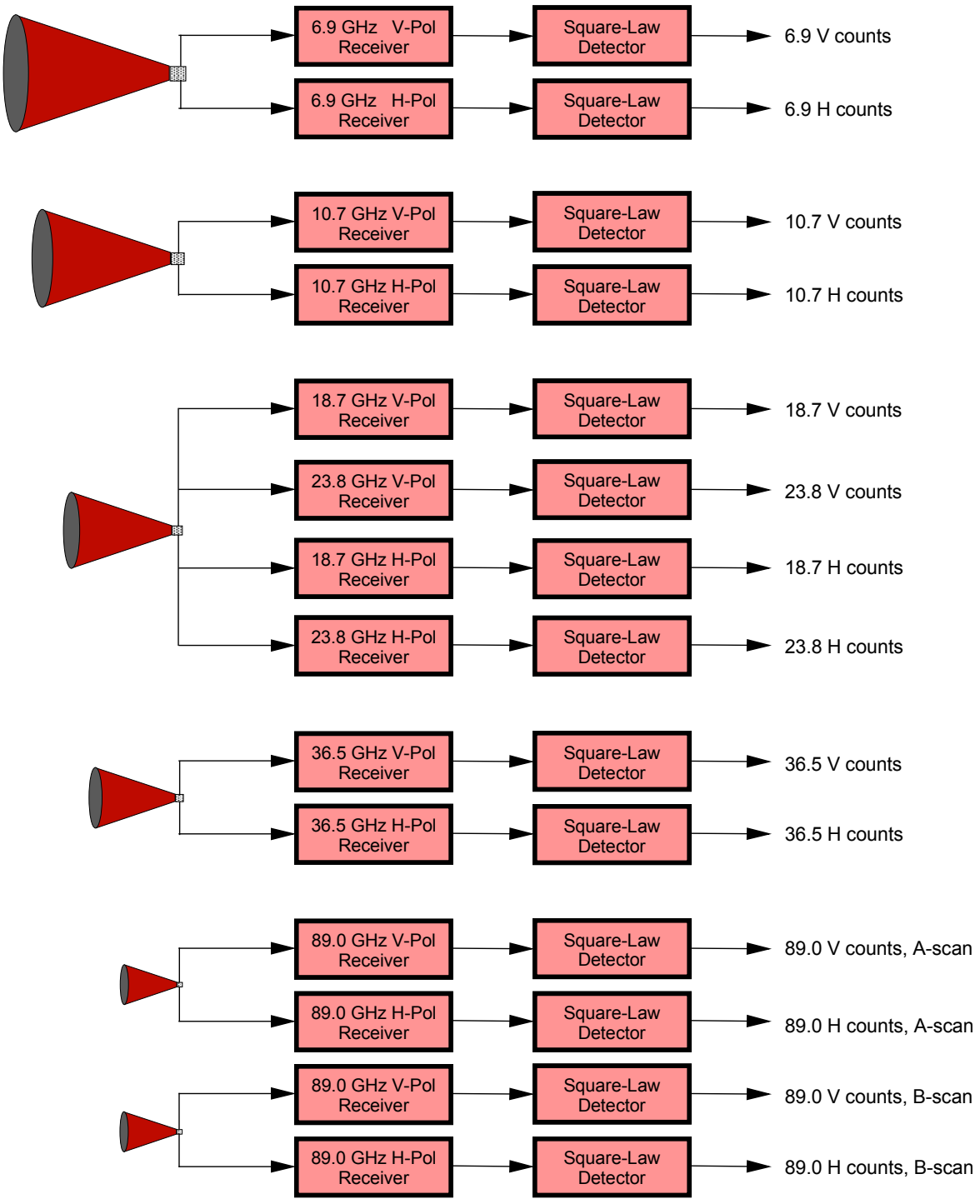

Figure 1: Block diagram for AMSR-E feedhorns and radiometers.

1.5 Level 2A Data Set

Although the Backus-Gilbert method could in principle be used to construct effective observations corresponding to gain patterns either larger or smaller than those of the actual observations, the noise amplification for construction of smaller gain patterns (deconvolution) was deemed unacceptable. In the interest of completeness, all actual brightness temperature observations derived directly from Level1A will be included (unchanged) as part of the Level2A data set. Consequently, all observations of the Level 2A data set are either unsampled actual observations (e.g., 37 GHz at Res. 4 and the 89 GHz at Res. 5), or constructions of larger gain patterns from multiple smaller patterns (spatial averaging). When the observations are spatially averaged, the resulting noise factor is always less than 1.

Table 2 describes the complete Level 2A data set, with such ancillary data as time, geolocation, and quality assessment under the heading of "misc." (Note that because the 18.7 and 23.8 GHz footprint are similar in size, both are described as "Resolution 3" although resampling will use the 18.7 GHz pattern.) Observation values are saved as unsigned integers with a scaling factor of 0.01 for all channels. The engineering values are obtained by multiplying by the scaling factor. The data volumes in the table correspond to 1.5 seconds of observation (1 complete scan). The data volume of 43,220 bytes for one scan implies a daily data rate of nearly 2500 MB.

An eight bit quality index is calculated for every observation at each resolution. Four of these bits indicate the fraction of the antenna pattern that is land, (weighted according to the gain pattern). When multiplied by the expected land-sea temperature difference, the result is the expected temperature error caused by land contamination. The user can then decide whether this amount of contamination is acceptable given the application of the data. The remaining 4 bits are reserved for future assignment.

In addition to conveying temperature information, the sixteen bits of each temperature data record also convey some quality control information. Completely missing T_B are denoted by a value of 0 K. This indicates that all relevant Level 1A data were missing. The temperature of 320 K is reserved for observations that are for whatever other reason unusable. Negative temperatures are used to signify observations that are somewhat questionable due to unreliability of at least one of the contributing Level 1A observations. Although these temperatures can probably be used safely, the negative temperature assignment is provided as a warning to the data user. The threshold that will differentiate the unusable observations that are labeled as 320 K from the observations that are given negative values has not yet been established.

Table 2: AMSR-E Level 2A Data Volumes

Data Item	Obj. No.	Bytes	Level1A Samples/scan	Level2A Samples/scan
Misc. overhead data		1	10292	14996
6.9V Res. 1 TB (K) (Unsampled)	1	2	294	294
6.9H Res. 1 TB (K) (Unsampled)	3	2	294	294
6.9V Res. 1 TB (K)	2	2	0	294
6.9H Res. 1 TB (K)	4	2	0	294
10.7V Res. 1 TB (K)	5	2	0	294
10.7H Res. 1 TB (K)	8	2	0	294
18.7V Res. 1 TB (K)	11	2	0	294
18.7H Res. 1 TB (K)	14	2	0	294
23.8V Res. 1 TB (K)	17	2	0	294
23.8H Res. 1 TB (K)	21	2	0	294
36.5V Res. 1 TB (K)	25	2	0	294
36.5H Res. 1 TB (K)	29	2	0	294
89.0V Res. 1 TB (K)	41	2	0	294
89.0H Res. 1 TB (K)	46	2	0	294
10.7V Res. 2 TB (K) (Unsampled)	6	2	294	294
10.7H Res. 2 TB (K) (Unsampled)	9	2	294	294
10.7V Res. 2 TB (K)	7	2	0	294
10.7H Res. 2 TB (K)	10	2	0	294
18.7V Res. 2 TB (K)	12	2	0	294
18.7H Res. 2 TB (K)	15	2	0	294
23.8V Res. 2 TB (K)	18	2	0	294
23.8H Res. 2 TB (K)	22	2	0	294
36.5V Res. 2 TB (K)	26	2	0	294
36.5H Res. 2 TB (K)	30	2	0	294
89.0V Res. 2 TB (K)	42	2	0	294
89.0H Res. 2 TB (K)	47	2	0	294
18.7V Res. 3 TB (K) (Unsampled)	13	2	294	294
18.7H Res. 3 TB (K) (Unsampled)	16	2	294	294
23.8V Res. 3 TB (K) (Unsampled)	20	2	294	294
23.8H Res. 3 TB (K) (Unsampled)	24	2	294	294
23.8V Res. 3 TB (K)	19	2	0	294
23.8H Res. 3 TB (K)	23	2	0	294
36.5V Res. 3 TB (K)	27	2	0	294
36.5H Res. 3 TB (K)	31	2	0	294
89.0V Res. 3 TB (K)	43	2	0	294
89.0H Res. 3 TB (K)	48	2	0	294
36.5V Res. 4 TB (K) (Unsampled)	28	2	294	294
36.5H Res. 4 TB (K) (Unsampled)	32	2	294	294
89.0V Res. 4 TB (K)	44	2	0	294
89.0H Res. 4 TB (K)	49	2	0	294
89.0V Res. 5 TB (K) (Unsampled)	45	2	1176	1176
89.0H Res. 5 TB (K) (Unsampled)	50	2	1176	1176
Total Bytes in scan (1.5 sec.)			20876	43220
Total Megabytes in orbit (99 min.)			82.67	171.15
Total Megabytes in day			1202.46	2489.47

Figure 2 is a schematic diagram illustrating the approximate geometry of the observations included in the Level 2A data set. The large antenna patterns in the figure indicate the locations of the Res. 1 through Res. 4 observations. The small patterns indicate the placement of the Res. 5 observations. Res. 1 through Res. 4 observations occur at 10 km intervals. The Res. 5 observations are on a 5 km spacing interleaved with the lower resolution observations.

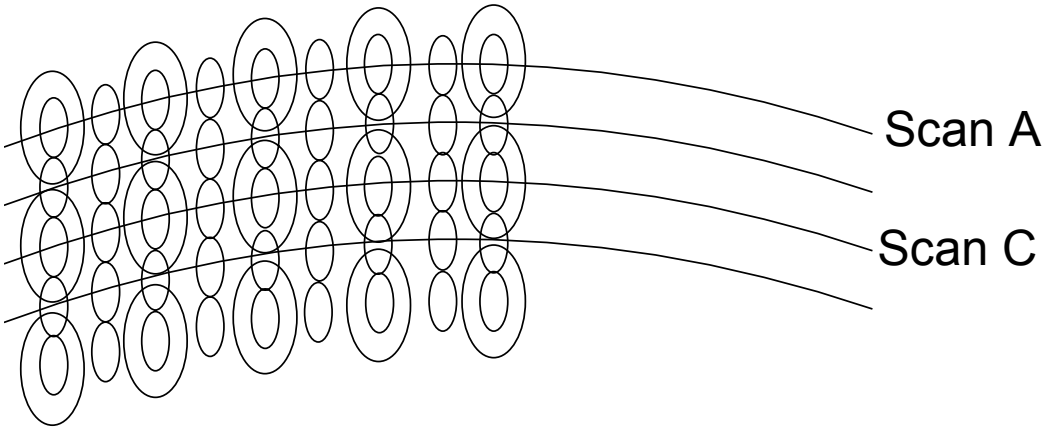

Figure 2: Geometry of observations from Level 2A data set. Scan A and Scan C are separated by approximately 10 km and follow sequential scans of the instrument (1.5 seconds apart).

2. Theoretical Basis of Algorithm

2.1 Introduction

The objective of the Level 2A algorithm is to bring the AMSR brightness temperature observations to a set of common spatial resolutions. In preparation for doing this, it is necessary to remove antenna spillover and cross-polarization effects from AMSR T_A observations. We include a discussion of spillover and cross-polarization correction here because of its extreme importance to the overall observation processing, even though it is not part of resampling per se. We also include a discussion of the effect of incidence angle variation over the antenna's main lobe. In Section 2.4 we then provide the Backus-Gilbert formulation for the Level 2A processing.

2.2 Removal of Antenna Spillover and Cross-Polarization Effects

Consider an antenna with a unit boresight vector $\mathbf{k_B}$ and unit polarization vector $\mathbf{p_B}$ (where $\mathbf{k_B} \cdot \mathbf{p_B} = 0$). For directions $\mathbf{k}$ away from $\mathbf{k_B}$, the polarization vector is given by

$$\mathbf{p} = (\mathbf{k_B} \times \mathbf{p_B}) \times \mathbf{k} \Big/ \left| (\mathbf{k_B} \times \mathbf{p_B}) \times \mathbf{k} \right| \tag{1}$$

A perfect antenna would be linearly polarized along $\mathbf{p}$. In reality, there is a small amount of cross-polarization leakage that produces elliptical polarization. It is generally assumed that the co-polarization and cross-polarization components are in phase such that the major axis of the ellipse is aligned with $\mathbf{p}$. For Earth-viewing radiometers, the boresight polarization vector $\mathbf{p_B}$ is generally aligned with either the Earth horizontal or vertical polarization vector, which are defined by

$$\mathbf{H} = \mathbf{N} \times \mathbf{k} / |\mathbf{N} \times \mathbf{k}| \tag{2}$$

$$\mathbf{V} = \mathbf{k} \times \mathbf{H} \tag{3}$$

where $\mathbf{N}$ is the unit normal to the Earth's surface at the point where the view vector $\mathbf{k}$ intersects the Earth. Note that $\mathbf{k}$ points downward and $\mathbf{N}$ points upward. Dual-polarization radiometers have two ports. The port for which $\mathbf{p_B}$ is aligned with $\mathbf{V}$ is called the v-pol port, and the port for which $\mathbf{p_B}$ is aligned with $\mathbf{H}$ is called the h-pol port. Note that off boresight the antenna polarization vector $\mathbf{p}$ is not aligned with either $\mathbf{V}$ or $\mathbf{H}$. This rotation of the antenna polarization vector with respect to the Earth polarization vectors is discussed below.

The amount of power received by the antenna from some specified differential solid angle is given by the antenna pattern. The co-pol pattern gives the received power that is polarized along $\mathbf{p}$, and the cross-pol pattern gives the received power that is polarized orthogonal to $\mathbf{p}$. We denote the co-pol pattern by G_{PP} and the cross-pol pattern by G_{PQ}. The first subscript P denotes the antenna port (either V or H), and the second subscript denotes the polarization of received power. We are using the subscript Q to denote the polarization orthogonal to P. When P = V, then Q = H, and vice versa. Typically G_{PQ} is 20 to 25 dB lower than G_{PP}. The gains are normalized such that the following integral

equals unity

$$\int_{E+S} d\Omega\left(G_{PP}+G_{PQ}\right)=1 \tag{4}$$

The E + S on the integral denotes that the integration is over both the earth and cold space (i.e., the full 4π steradians). The gains G_{PP} and G_{PQ} are implicit functions of the solid angle Ω. The antenna temperature received by the antenna is [*Claassen and Fung*, 1974]

$$\begin{aligned} T_{AP} = &\int_{E} d\Omega\left[G_{PP}\left(T_{BP}\cos^2\varphi + T_{BQ}\sin^2\varphi\right) + G_{PQ}\left(T_{BQ}\cos^2\varphi + T_{BP}\sin^2\varphi\right)\right] \\ &+\int_{S} d\Omega\left(G_{PP}+G_{PQ}\right)T_{BC} \end{aligned} \tag{5}$$

where we have partitioned the integral into two regions: the Earth and cold space. The Earth brightness temperatures T_{BP} and T_{BQ} are implicit functions of Ω, and the cold space brightness temperature T_{BC} is a constant. The angle φ is the angle made the antenna polarization vector **p** and the Earth polarization vector **P** (where **p** and **P** are the same polarization).

The cold-space contribution is subtracted from T_{AP} and the antenna gains are renormalized. The resulting quantity T'_{AP} is called the Earth antenna temperature.

$$T'_{AP} = \Lambda_P^{-1}\left[T_{AP} - \left(1-\Lambda_P\right)T_{BC}\right] \tag{6}$$

$$\Lambda_P = \int_{E} d\Omega\left(G_{PP}+G_{PQ}\right) \tag{7}$$

The term $1 - \Lambda_P$ is commonly called the spillover factor and can be measured in the field. Combining (5) and (6) gives

$$T'_{AP} = \Lambda_P^{-1}\int_{E} d\Omega\left[G_{PP}\left(T_{BP}\cos^2\varphi + T_{BQ}\sin^2\varphi\right) + G_{PQ}\left(T_{BQ}\cos^2\varphi + T_{BP}\sin^2\varphi\right)\right] \tag{8}$$

We now make an approximation based on the fact that the AMSR antenna patterns are narrow. The AMSR 6.9 GHz channels have the largest 3-dB full beam width, which is about 2.2°. Over the main lobe of the antenna pattern, which is about 2.5 times the 3-dB beam width, the polarization rotation angle φ ranges from 0° to a maximum value of 2°. Thus a good approximation for AMSR is to set φ to 0° in (8). Simulations show the error in setting φ to 0° is a maximum of 0.03K in T'_{AP}.

Apart from a scaling factor, the general shape of the cross-pol gain is similar to the co-pol gain, and accordingly we make use of the following expression:

$$G_{PQ} = \chi_P(1-\chi_P)^{-1}G_{PP} + \varepsilon_P \tag{9}$$

$$\chi_P = \Lambda_P^{-1}\int_{E} d\Omega\, G_{PQ} \tag{10}$$

The first term of (9) is a scaled down version of the co-pol gain and ε_P accounts for deviations of G_{PQ} from the shape of the co-pol gain. These deviations may include a

quasi-null at boresight and relatively high sidelobes. The term χ_P is cross-polarization leakage. It is a measure of the total cross-pol power divided by the total power (both co-pol and cross-pol), which can be measured in the field. Preliminary estimates of the AMSR antenna patterns indicate that χ_P will be about 1%. The normalization in (9) is such that

$$\int_E d\Omega \; \varepsilon_P = 0 \tag{11}$$

Setting φ to 0° and substituting (9) into (8) gives

$$T'_{AP} = \Lambda_P^{-1} \int_E d\Omega \; G_{PP}\left(T_{BP} + \chi_P\left(1-\chi_P\right)^{-1} T_{BQ}\right) + \Lambda_P^{-1} \int_E d\Omega \; \varepsilon_P T_{BQ} \tag{12}$$

In general, the second integral represents a very small zero-mean error, which will be essentially zero if the variations in Earth brightness temperature are uncorrelated with the variations in ε_P. To determine the worst-case magnitude of the ε_P term, we integrate $|\varepsilon_P|$ as computed from preliminary AMSR antenna patterns and find

$$\int_E d\Omega \; \left|\varepsilon_P\right| \; \approx \; 0.005 \tag{13}$$

If the T_B variations over the main lobe that are correlated with ε_P are 5 K, then the second integral will contribute 0.025 K to T'_{AP}. We consider this to be a worst case, and hence we set the second integral to zero.

Dual polarization radiometers generally have the property that the v-pol and h-pol co-pol gains are very similar. In view of this, we make use of the following expression to relate G_{PP} and G_{QQ}:

$$G_{PP} = \left[\Lambda_P\left(1-\chi_P\right)\right]\left[\Lambda_Q\left(1-\chi_Q\right)\right]^{-1} G_{QQ} + \varepsilon \tag{14}$$

where the leading factors properly normalize G_{PP} such that the integral of error ε is zero, analogous to (11) above. Substituting (14) into (12) gives

$$\begin{aligned} T'_{AP} = {} & \Lambda_P^{-1} \int_E d\Omega \; G_{PP} T_{BP} + \Lambda_Q^{-1} \chi_P \left(1-\chi_Q\right)^{-1} \int_E d\Omega \; G_{QQ} T_{BQ} \\ & + \Lambda_P^{-1} \chi_P \left(1-\chi_P\right)^{-1} \int_E d\Omega \; \varepsilon T_{BQ} \end{aligned} \tag{15}$$

As was the case above, the last integral is a very small zero-mean error that goes to zero if variations in ε and T_{BQ} are uncorrelated. We set this term to zero.

Let $\overline{T}_{BP}$ denote the Earth brightness temperature integrated over the co-pol antenna pattern.

$$\overline{T}_{BP} = \Lambda_P^{-1}\left(1-\chi_P\right)^{-1} \int_E d\Omega \; G_{PP} T_{BP} \tag{16}$$

The leading factors normalized G_{PP} such that its integral over the Earth equals unity. Substituting (16) in (15) gives

$$T'_{AP} = (1-\chi_P)\overline{T}_{BP} + \chi_P \overline{T}_{BQ} \tag{17}$$

Equation (17) represents two simultaneous equations, one for P = V and the other for P = H. Solving these two equations yields

$$\overline{T}_{BP} = T'_{AP} + \chi_P (1-\chi_P-\chi_Q)^{-1}(T'_{AP} - T'_{AQ}) \tag{18}$$

which holds for both P = H and P = V.

In summary, the antenna temperature observations are first corrected for cold-space spillover using equation (6) to obtain the Earth antenna temperature. Equation (18) is then used to remove the effect of the cross-polarization. The final result is the Earth brightness temperature $\overline{T}_{BP}$ averaged over the normalized co-pol antenna pattern. This procedure requires two antenna pattern measurements: the spillover factor $1 - \Lambda_P$ and the cross-polarization leakage χ_P. We expect that the major source of error in computing $\overline{T}_{BP}$ will be due to the error in measuring $1 - \Lambda_P$ and χ_P in field, rather than the error in the numerical approximations used above.

2.3 Incidence Angle Variation over the Main Lobe

The Earth brightness temperature depends on the antenna view direction, which is specified in terms of two angles: the incidence angle θ and the azimuth angle ϕ. The incidence angle is the angle made by the viewing vector **k** and the normal vector **N** to the Earth's surface:

$$\theta = \arccos(-\mathbf{k}\cdot\mathbf{N}/|\mathbf{k}\cdot\mathbf{N}|) \tag{19}$$

The azimuth angle is the angle made by the projection of **k** onto the Earth surface relative to north. At 6.9 GHz, over the main lobe of the antenna, θ and ϕ vary by about ± 2°. The variation of T_B with ϕ is typically quite small. For example, the ocean shows a maximum peak-to-peak variation of about 5 K over 180°, which corresponds to less than a ±0.1 K variation over the main lobe. Hence the ϕ variation can be neglected. However, the θ variation is more significant. Over the ocean with clear skies, the v-pol T_B increases by about 2 K per degree increase in θ. To analyze the effect of the θ variation, we use the following model for the T_B versus θ dependence over the main lobe of the antenna.

$$T_B = T_{BO}(1 + h_1\Delta\theta + h_2\Delta\theta^2) \tag{20}$$

where T_{BO} is the brightness temperature measured at the boresight incidence angle, Δθ is the difference between the local incidence angle and the boresight incidence angle, and h is a constant. Substituting (20) into (16) gives (the P subscripts are now implicit)

$$\overline{T}_B = \int_E d\Omega\ \overline{G}T_{BO} + \int_E d\Omega\ \overline{G}T_{BO}h_2\Delta\theta^2(1+h_1\Delta\theta)^{-1} \tag{21}$$

$$\overline{G} = \Lambda^{-1}(1-\chi)^{-1}G(1+h_1\Delta\theta) \tag{22}$$

where the incidence angle dependence has been lumped into the antenna gain. Simulation shows that the integral of $G\Delta\theta$ is essentially zero, so $\overline{G}$ retains its proper

normalization. The first integral is normalized so that if T_{BO} is constant over the antenna pattern, then $\overline{T}_B = T_{BO}$. The second integral represents a small bias term due to the non-linear part of the T_B versus θ relationship. The value of the bias depends upon the surface type and polarization. The worst case is a v-pol observation of the ocean under clear skies for which the bias is about + 0.1 K. When doing the geophysical processing, this bias is subtracted from $\overline{T}_B$, thereby leaving just the first integral in (21). This integral has the important property that the brightness temperature T_{BO} depends only on Earth location and not on the viewing direction. This property along with the fact that $\overline{G}$ is properly normalized are necessary conditions for the spatial resolution matching techniques to be discussed in the next section.

2.4 Mathematical Description of Level 2A Algorithm

For simplicity, the notation used in the remainder of the discussion is slightly modified from that used earlier. In addition to dropping the polarization subscript, a new subscript *i* is added to brightness temperatures and antenna gain patterns to differentiate between observations. Finally, the leading constants of equation (16) are absorbed into the expression for the gain pattern, and each observation is expressed as an integration over a surface area rather than an integration over a solid angle. In summary then, using the substitution

$$G_i \leftarrow \Lambda^{-1}(1-\chi)^{-1}\frac{\cos\theta}{r^2}G_{PP} \tag{23}$$

equation (16) can be rewritten so that an observed antenna temperature centered at location ρ_0 can be expressed as

$$\overline{T}_{Bi} = \int T_B(\rho)G_i(\rho)\,dA \tag{24}$$

where $T_B(\rho)$ is the brightness temperature of the Earth at some location ρ, and $G_i(\rho)$ is the antenna gain pattern corresponding to the specific observation. The constructed brightness temperature $\hat{T}_B$ is defined as a weighted sum of actual observations

$$\begin{aligned}\hat{T}_B &= \sum_{i=1}^{N} a_i \overline{T}_{Bi} \\ &= \int T_B(\rho)\sum_{i=1}^{N} a_i G_i(\rho)\,dA\end{aligned} \tag{25}$$

The challenge is to choose weighting coefficients a_i such that the constructed brightness temperature $\hat{T}_B$ and the effective antenna pattern $\sum_{i=1}^{N} a_i G_i(\rho)$ have desirable characteristics. The ideal effective antenna pattern should closely match some specified target pattern, and minimally amplify noise. In general, these two objectives are incompatible, requiring some compromise. The Backus-Gilbert method accomplishes this compromise by providing a solution vector **a** of weights that minimize a sum of the integrated squared error in the fit, and variance due to noise amplification. Adapting the notation of Stogryn, this sum can be expressed as

$$Q = Q_0 + e^2 w\beta, \tag{26}$$

and is minimized subject to the normalizing constraint that

$$\int \sum_{i=1}^{N} a_i G_i(\rho) dA = 1. \tag{27}$$

In this formulation,

$$Q_0 = \int \left[\sum_{i=1}^{N} a_i G_i(\rho) - F(\rho) \right]^2 J(\rho) dA \tag{28}$$

is a measure of how well the constructed pattern matches a desired pattern $F(\rho)$. (The integral of $F(\rho)$ is normalized to 1). The variance of the weighted sum $\hat{T}_B$ due to measurement errors on the $\overline{T}_{Bi}$ is $e^2 = \mathbf{a}^{\mathrm{T}}\mathbf{E}\mathbf{a}$, where $\mathbf{E}$ is the error covariance matrix of the actual measurements. (In other words, error in $\hat{T}_B$ resulting from measurement noise is proportional to the noise amplification factor $n_f = \sqrt{\mathbf{a}^{\mathrm{T}}\mathbf{a}}$ under the working assumption that measurement errors for each observation of a given channel are equal and independent, i.e., $\mathbf{E} = \mathbf{I}\sigma^2$.) A smoothing parameter β ranges from 0 to infinity, and w is a scaling factor. The value of the smoothing parameter reflects the importance of achieving a good fit relative to the importance of minimizing amplification of measurement noise. For simplicity, the scaling factor w was set to unity for our calculations, effectively giving β the combined role of both scaling factor and smoothing parameter. This convention does not impose any additional restriction on the set of possible solutions to the minimization problem.

In general, the vector of weighting coefficients that minimizes Equation (26) subject to constraint (27) is

$$\mathbf{a} = \mathbf{V}^{-1}\left[\mathbf{v} + \left(\frac{1 - \mathbf{u}^{\mathrm{T}}\mathbf{V}^{-1}\mathbf{v}}{\mathbf{u}^{\mathrm{T}}\mathbf{V}^{-1}\mathbf{u}} \right)\mathbf{u} \right] \tag{29}$$

where

$$\mathbf{V} = \mathbf{G} + w\mathbf{E}\beta \tag{30}$$

$$u_i = \int G_i(\rho)\, dA \tag{31}$$

$$v_i = \int G_i(\rho) F(\rho) J(\rho)\, dA \tag{32}$$

$$G_{ij} = \int G_i(\rho) G_j(\rho) J(\rho)\, dA. \tag{33}$$

Investigation revealed that the benefit of using the weighting factor $J(\rho)$ to suppress sidelobes was small, while the resulting distortion to the main lobe of the constructed pattern was significant. Consequently, the weighting factor was set to unity throughout this application.

3. Calculation of Weighting Coefficients

3.1 Introduction

Calculation of weighting coefficients requires specification of the shape of the target pattern, the location of the target pattern relative to the actual measurements, the set of actual observations used, and the smoothing parameter for each constructed observation. In general, actual observations within an 80 km radius of the constructed pattern are considered for possible contributors to the construction. An 80 km radius is chosen because it is larger than even the largest of the target patterns (Res. 1). Of the many observations within the 80 km radius, those that are too far from the target pattern to play a role in the construction are assigned a weight of zero by the algorithm. Thus, the only cost to having an excessively large search radius is computation time, not accuracy.

Weighting coefficients are computed on the basis of simulation of the antenna patterns for a portion of a circular orbit around a spherical Earth. Sensitivity analysis will demonstrate that the weights produced through the simulation are appropriate for the actual (slightly elliptical) orbit around the slightly oblate Earth.

3.2 Target Patterns

As stated earlier, the target patterns used to compute the Resolution 1 through 4 observations of the Level 2A data set correspond to the footprint sizes of the 6.9, 10.7, 18.7, and 36.5 GHz antenna patterns. (The 89 GHz data are derived directly from the Level 1A data set, without spatial averaging.) Each of the constructed patterns is centered at the location of an actual observation. For example, the calculated 6.9 GHz patterns with a spacing of approximately 10 km fall on sites of the actual Level 1A 6.9 GHz observations, which also have a spacing of approximately 10 km.

The target gain patterns should match the actual AMSR antenna patterns. Currently, the target gain patterns as well as the actual observation gain patterns are modeled as uniform plane waves diffracted by a circular aperture representing the antenna. The antenna patterns will be modified in the future to match actual AMSR antenna pattern measurements when they become available.

The antenna patterns are currently sampled on a grid with a spatial resolution ranging from 4 km in the case of the 6.9 GHz patterns, to 1 km for the 37 GHz patterns. The number of samples resulting from these sampling resolutions greatly exceeds the number of points at which the actual patterns will be characterized through pre-launch antenna pattern measurements. Thus, this resolution is more than sufficient to capture our current knowledge of the actual antenna patterns.

3.3 Tradeoff Analysis: Choice of Smoothing Parameter

As stated earlier, error on a constructed observation $\hat{T}_B$ arises from two sources. The

first source of error is mismatch between the ideal antenna pattern and the construction. The error in $\hat{T}_B$ due to pattern mismatch can be described by the following equation.

$$E_1 = \int \left[\sum_{i=1}^{N} a_i G_i(\rho) - F(\rho) \right] T_B(\rho)\, dA \tag{34}$$

Although the expectation of E_1 is 0, the variance of E_1 depends on the spatial statistics of the actual temperature field $T_B(\rho)$. For example, the simplest case of a constant temperature field would result in $E_1 = 0$ even if the constructed pattern bore little resemblance to the desired pattern. Alternatively, Equation (28) would be proportional to the fit error if the power spectral density of $T_B(\rho)$ were uniform [*Poe*, 1990]. Unfortunately, an actual temperature field will match neither of these convenient cases.

The second source of error is random measurement error. The variance of $\hat{T}_B$ due to random measurement error is independent of the actual temperature field, depending only on the weighting coefficients and the observation error of each observation $\overline{T}_{Bi}$. (See the discussion of the noise factor n_f in Section 2.4.) For this reason, the effect of random measurement error is more easily quantified than the effect of fit error.

The two types of error cannot be directly compared (or added), except contingent on specific assumptions about the spatial characteristics of the actual temperature field $T_B(\rho)$. One approach is to use actual high-resolution observations to represent $T_B(\rho)$. Poe [1990], Robinson et al. [1992], Farrar and Smith [1992], and Farrar et al. [1994] used this approach. Another approach is to simulate $T_B(\rho)$. Robinson et al. [1992] used a circular pattern for this purpose.

Integrating the absolute value of the fit error provides what might be considered a "worst case" measure of the effect of pattern mismatch. Throughout the remainder of this discussion and in the figures that follow, this scalar value is used as a measure of the fit. This measure was chosen in order to avoid any possibility that mismatched areas of opposite sign might misleadingly produce an apparently small error through cancellation.

Although the smoothing parameter can be set to zero (see Poe [1990] for example), specification of a nonzero value allows judicious tradeoff of the noise reduction benefits of multiple observations versus the need to maintain a good fit. Figure 3 illustrates this tradeoff for one specific Level 2A data product at various observation positions along the scan. While other data products will differ in detail from this example, the general principle is that increased smoothing reduces the noise factor while degrading the fit. For this data product, this tradeoff is most conspicuous at the edges of the scan, whereas the combination of fit and noise factor selected nearer the center of the scan is essentially optimized for fit. In addition to generally determining the tradeoff of fit versus the noise factor, even a very small amount of smoothing produces the additional benefit of stabilizing the matrix inversions against roundoff error without otherwise affecting the calculated weighting coefficients.

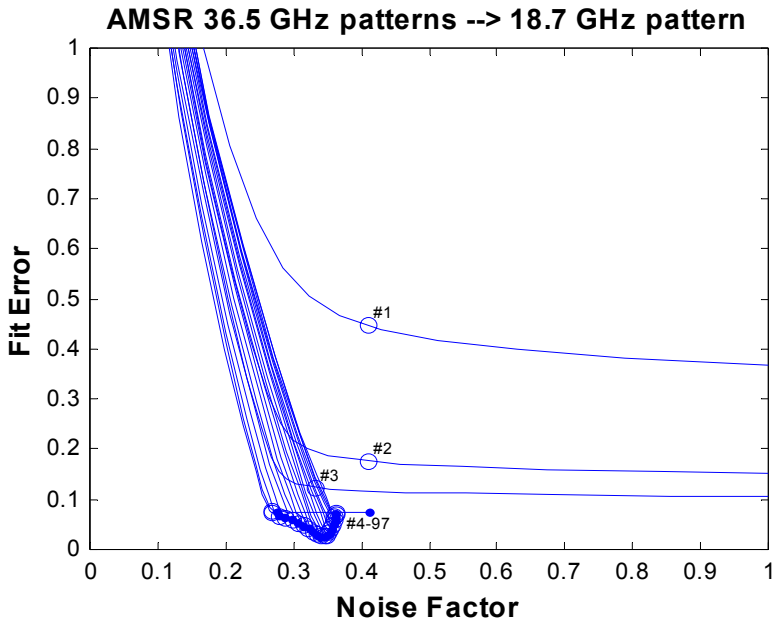

Figure 3: Tradeoff of noise factor and fit as a function of smoothing parameter for various scan positions for one specific Level 2A data product. Each open circle indicates the combination of fit and noise factor selected for that scan position. The end of each line corresponds to no smoothing – minimized fit error.

The following considerations should guide the choice of a smoothing parameter. It is generally counterproductive to construct an antenna pattern that is more "accurate" than necessary at the expense of increased noise factor. Thus one guideline for choice of the smoothing factor is that the mismatch between the constructed pattern and the target pattern should not be smaller than the uncertainty in the target pattern. Another guideline is that the constructed pattern should not have negative values. This is not anticipated to be a problem in these averaging applications, but it would be a significant concern for deconvolution. Another guideline is that the noise factor should not exceed 1. This too would be a greater concern for deconvolution than for averaging.

In the center of the scan, an amount of smoothing is chosen that allows nearly the best possible fit for that combination of frequencies. The only exceptions to this rule occur when the frequency of the actual observations matches the frequency of the ideal pattern that is being constructed. In those cases, the best possible fit is theoretically perfect, (i.e., giving full weight to the center observation and ignoring all the others). In those cases, a small amount of smoothing is chosen resulting in a fit error of less than 2%.

Figure 4 illustrates the ideal gain pattern, the reconstruction, and the difference between the two for the Res. 3 pattern generated from 37.5 GHz patterns. In this example, the location of the construction (the center of the scan or observation number 98) and combination of channel number match those of Figure 3. The smoothing parameter chosen is $\beta = 0.0001$. Consistent with the preceding paragraph, this amount of smoothing permits nearly the best fit possible for this set of actual observations while allowing a reasonable amount of noise reduction. Note that the difference plot extends

somewhat beyond what might usually be considered the extent of the actual ideal antenna pattern. This effect is one result of the fact that a large number of observations are combined to produce the reconstruction.

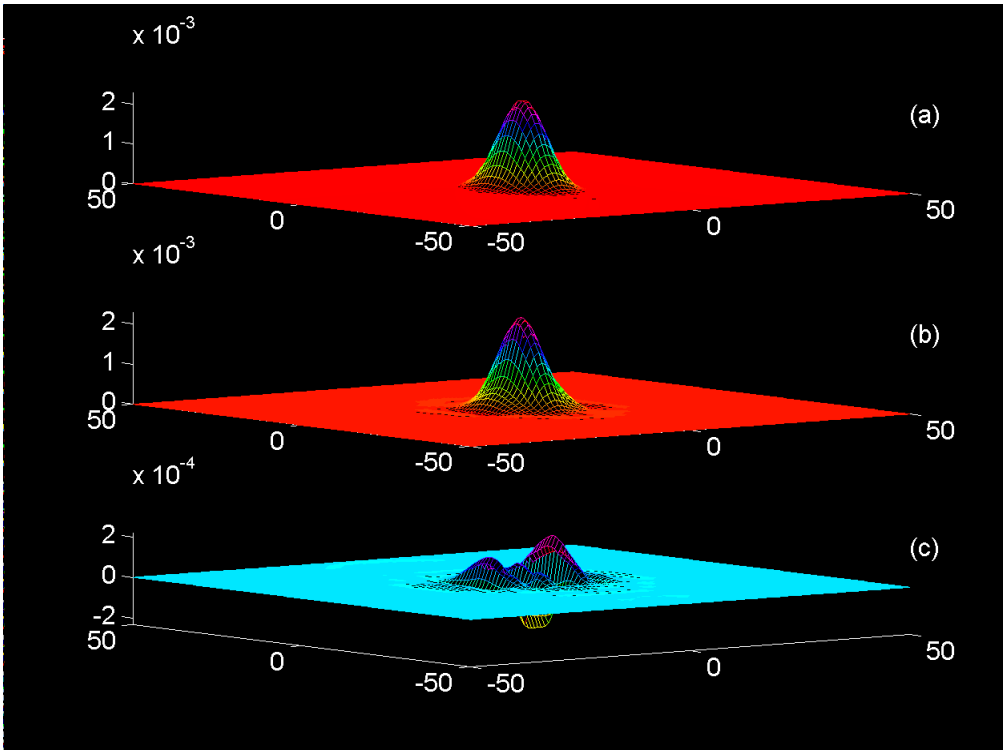

Figure 4: Example comparison of ideal antenna pattern with constructed. (a) is the ideal, (b) is the constructed version, and (c) is the difference. Note that the vertical scale of (c) is exaggerated by a factor of five relative to (a) and (b).

For a specified observation frequency and a specified target pattern, the smoothing parameter used to produce the constructed pattern need not be constant across the entire scan. Instead, it is desirable to adjust the smoothing parameter through the course of a scan to take advantage of the generally increasing density of observations away from the center of the scan, or to compensate for the fact that observations are not available beyond the scan edge. Adjustment of the smoothing parameter throughout the scan can thus result in a nearly constant noise factor across the entire scan.

The smoothing factor at each position across the scan of each Level 2A data set is chosen in the following way. The amount of smoothing applied at the center is also applied for observations closer to the edges. The general effect of maintaining a constant smoothing factor is that the noise factor decreases as the spatial density of the actual observations increases towards the edges. This trend holds true until the extreme edges of the scan, at which point the fit must degrade because the patterns to be constructed extend beyond the area in which observations were actually obtained. For construction of observations at the extreme edges of the scan, sufficient smoothing is added to keep the

noise factor from exceeding the value at the center. Figure 5 shows the fit and noise factor across an entire scan for one specific case, (in this case, the same combination of frequencies illustrated in Figure 3 and Figure 4).

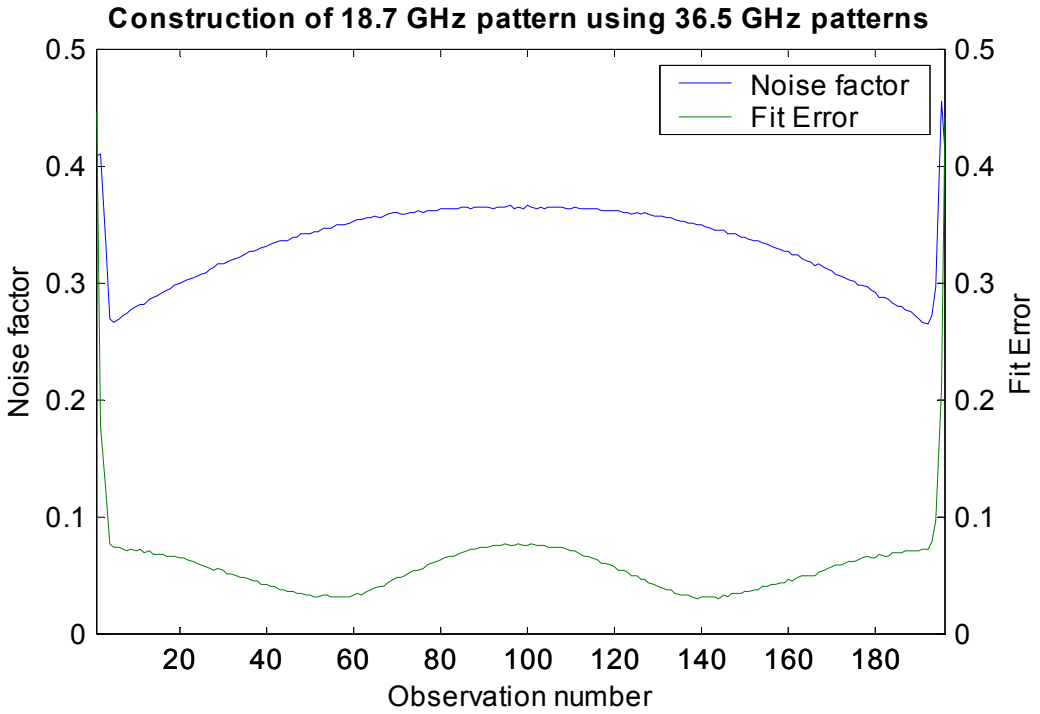

Figure 5: Noise factor and integrated magnitude of error between actual antenna pattern and interpolation across a single scan from -61° to +61° for a single data product.

The noise factor and fit of each of the Level 2A objects at the center of the scan is shown in Table 3. As in Table 2, Resolutions 1 through 5 correspond to the footprint sizes of the 6.9, 10.7, 18.7, 36.5, and 89 GHz observations. Note that the integrated fit error is small in every case, and that the noise factor is often significantly less than 1. The vertically and horizontally polarized gain patterns for each frequency are currently modeled identically, but that will not necessarily remain true if more accurate measurements of actual antenna patterns become available. Also note that for a given Level 1A channel, the noise factor decreases as the resolution of the constructed pattern becomes larger and the number of useful actual observations increases.

Table 3: Noise Factor and Fit of Constructions at Center of Scan.

Data Item	Object Nos.	Noise Factor	Fit Error
6.9 GHz to Res. 1	2, 4	.349	.034
10.7 GHz to Res. 1	5, 8	.149	.039
18.7 GHz to Res. 1	11, 14	.130	.043
23.8 GHz to Res. 1	17, 21	.127	.059
36.5 GHz to Res. 1	25, 29	.126	.088
89.0 GHz to Res. 1	41, 46	.062	.141
10.7 GHz to Res. 2	7, 10	.481	.063
18.7 GHz to Res. 2	12, 15	.217	.040
23.8 GHz to Res. 2	18, 22	.204	.034
36.5 GHz to Res. 2	26, 30	.196	.061
89.0 GHz to Res. 2	26, 30	.094	137
23.8 GHz to Res. 3	19, 23	.469	.041
36.5 GHz to Res. 3	27, 31	.367	.082
89.0 GHz to Res. 3	43, 48	.161	.151
89.0 GHz to Res. 4	44, 49	.309	.153

3.4 Simulation Characteristics

Weighting coefficients are calculated assuming a spherical Earth and a circular orbit. The Earth was assumed to have a radius of 6367 km, and the instrument altitude was assumed to be 705 km. Actual observation geometry will vary slightly as a result of oblateness of the Earth, and the elliptical instrument orbit. The effects of these factors on variations in the distance between successive scans and the distance between observations within a scan are described below. Section 3.5 summarizes the reasoning used to demonstrate that the weighting coefficients obtained for the nominal orbital case are applicable generally.

3.4.1 Altitude

Figure 6 illustrates the instrument altitude throughout an entire orbit for perigee angles of 0°, 45°, and 90°. The figure confirms the nominal altitude of 705 km, and shows that the Level 2A algorithm must function over a range of approximately ±25 km. Because variations in altitude modify both the spacing between the observations and the antenna patterns themselves, the first order effect of changes in altitude is merely to scale the actual and reconstructed antenna patterns rather than to degrade the fit.

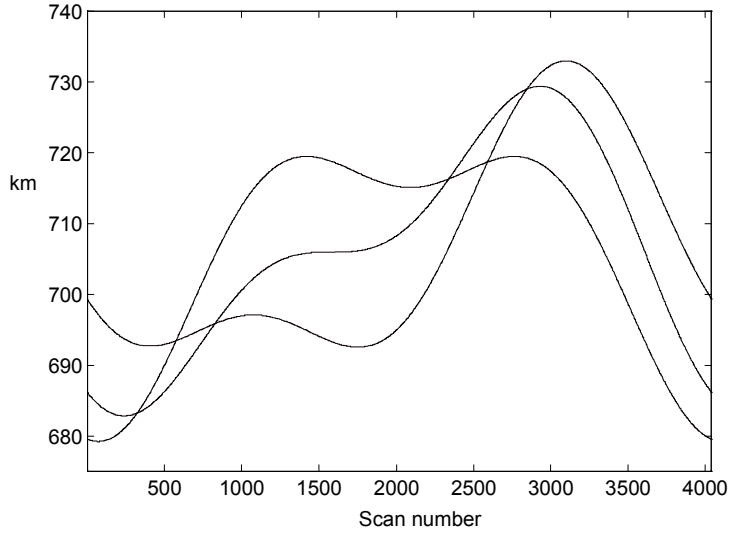

Figure 6: Instrument altitude throughout an entire orbit for three different perigee angles (t_0=0°,45°,90°).

3.4.2 Distances between observations within scan

Figure 7 illustrates the distance between adjacent AMSR observations within single scans from -61° to +61° when the instrument is in a polar orbit passing over the equator. The three lines correspond to scans 27 seconds ahead and 27 seconds behind a scan centered at the equator, as well as the centered scan. The two most significant causes of variation in the distance between adjacent observations are movement of the instrument during the scan, and oblateness of the Earth. These two factors have effects of approximately equal magnitude. The effect of Earth rotation is essentially constant over the scan. A spacing of 27 seconds was chosen as a worst case, corresponding to the time necessary for 18 scans, or approximately three times the beamwidth of the 6.9 GHz gain pattern.

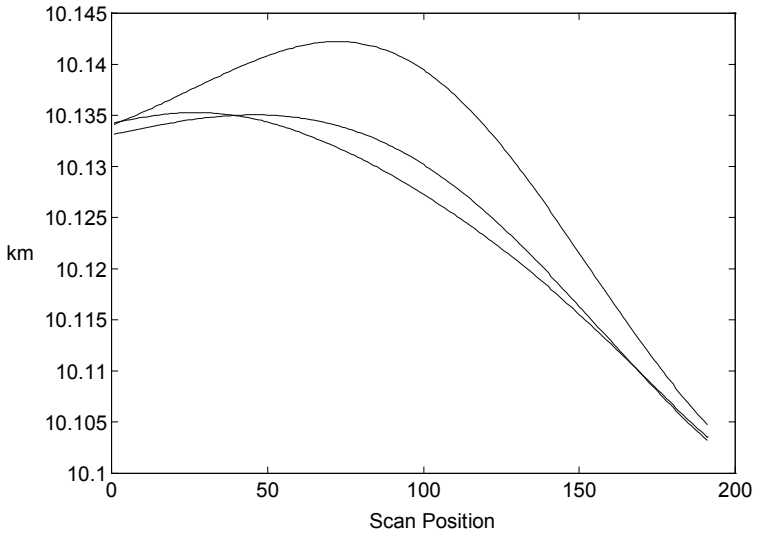

Figure 7: Distance (km) between adjacent observations within single AMSR scans centered at the equator as well as 27 seconds ahead and behind.

3.4.3 Distances between scans

The spacing between scans varies in the course of a complete orbit, and differs among the observations within a scan. These differences arise for the following reasons.

1. The elliptical satellite orbit would cause variations in the inter-scan distance even for a spherical Earth.
2. The oblateness of the Earth superimposes further variations with some relative phase determined by the orientation of the major axis of the satellite orbit relative to the Earth axis.
3. Inter-scan distance is generally greater when measured at the middle of the scan than at the edges because the total distance covered in an orbit is greater at the middle of the scan.
4. Earth rotation causes an asymmetry between the inter-scan distance measured at the first observation of each scan, and that measured at the last observation of each scan.

The combined effect of all these considerations is shown in Figure 8 through Figure 10 for 20 different observation positions across the scan. These figures differ only in the perigee angle of the satellite orbit. For the cases depicted, the maximum rate of change in inter-scan distance is approximately 0.35 m/scan. Also, the maximum range of inter-scan distances within any orbit is approximately 200 m.

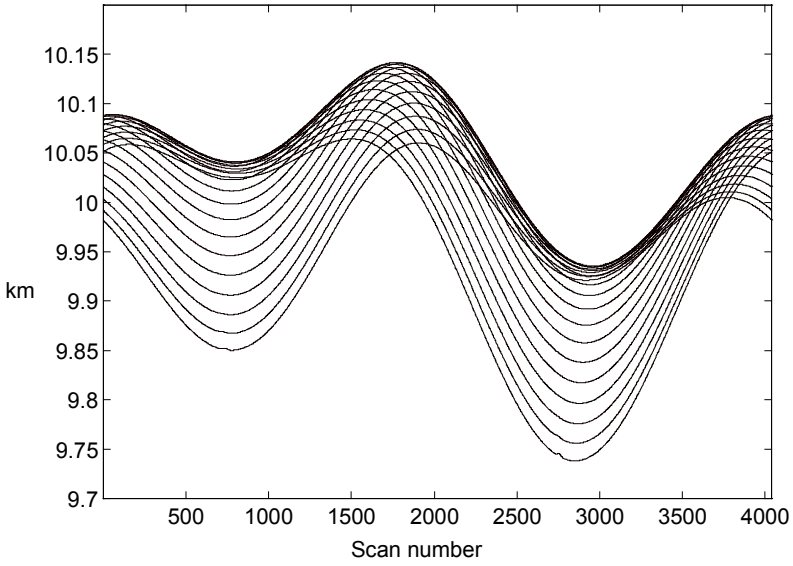

Figure 8: Distance between subsequent scans throughout an entire orbit measured at 20 different observation positions (t_0=90°).

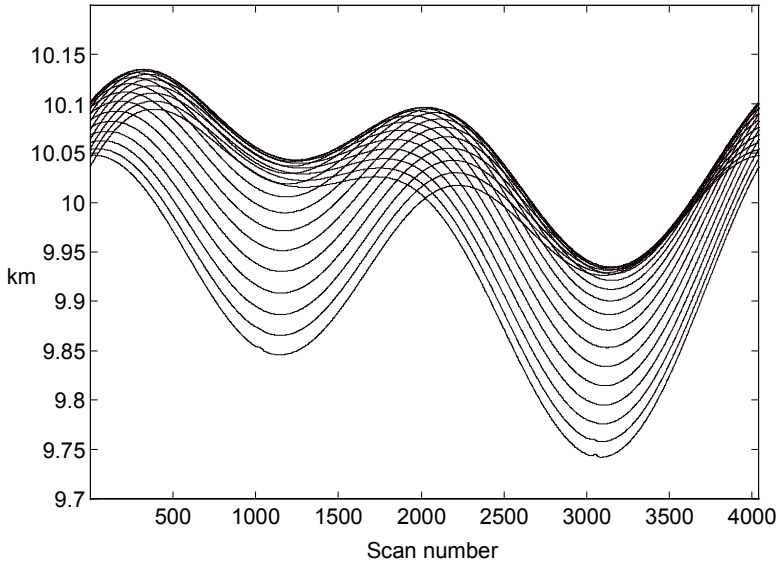

Figure 9: Distance between subsequent scans throughout an entire orbit measured at 20 different observation positions (t_0=45°).

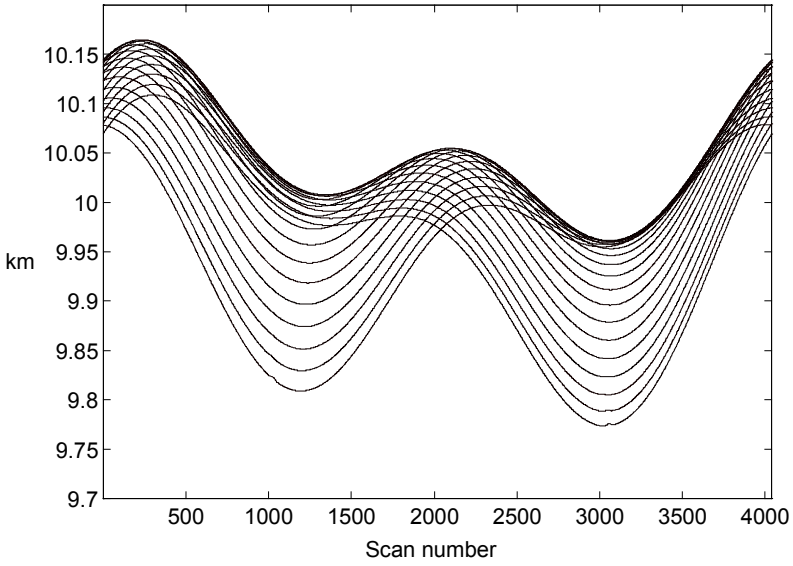

Figure 10: Distance between subsequent scans throughout an entire orbit measured at 20 different observation positions (t_0=0°).

In summary, the distance between adjacent scans is consistent to within ± 0.2 km, and the distance between adjacent observations within a scan is consistent to within ± 0.02 km. The altitude is consistent to within ± 25 km.

3.5 Sensitivity of Constructed Observations

The sensitivity analysis must consider two issues in order to demonstrate that the weighting coefficients derived from simulations using one portion of one simplified orbit are applicable to observations in general, (despite the fact that actual orbits are slightly elliptical and the Earth is slightly oblate). The first issue is that some aspect of the platform, (e.g., altitude or attitude), might differ from the nominal case simulation. The second aspect is that the assumed antenna patterns might not match the actual antenna patterns. Thus, this portion of the sensitivity analysis must demonstrate that neither the model used to generate the weighting coefficients, nor differences in the antenna pattern after launch introduce significant fit error. Ultimately, the most relevant question is not the effect of these differences on the derived weighting coefficients, but the resulting fit error of the reconstructed antenna patterns. This sensitivity analysis has not yet been completed.

3.5.1 Sensitivity to orbital characteristics

The variation of altitudes over the range depicted in Figure 6, and the resulting range of inter-observational distances indicated by Figure 7 through Figure 10 should have very little effect on the fit of the constructed pattern. Rather than demonstrate this insensitivity for all observations of all Level 2A channels, it will be sufficient to examine a representative case. Those channels most sensitive to variations in the spacing of

observations are those in which a small footprint is constructed from a number of still smaller footprints. For example, objects 44 and 49 from Table 3 would be more susceptible to this problem than other resampled channels.

3.5.2 Sensitivity to antenna pattern

Pre-launch measurements of the actual antenna pattern are used to simulate antenna patterns that eventually allow computation of weighting coefficients. Despite antenna pattern measurements conducted prior to launch, the actual antenna patterns when the instrument is deployed are only imperfectly known.

4. Implementation Issues

4.1 Introduction

Weighting coefficients are applied by reading an entire file (one half orbit) of Level 1A data at a time. Tables of weighting coefficients are then used to generate the Level 2A constructed measurements as shown in Equation (25). In implementation, the weighting coefficients corresponding to each constructed observation are stored as a (29×29) array, allowing for weights to be applied to actual observations ± 14 scans and ± 14 locations along the scan from the constructed observation. These dimensions were chosen so that a single array size would accommodate any location of any of the Level 2A data products. In any particular case, many of the coefficients in the array will be zero. Ideally, application of weighting coefficients is a straightforward process of applying the weighting coefficients corresponding to each constructed pattern within the scan, and repeating the process for each of the scans throughout the orbital record. Several considerations may complicate the process, and these issues are discussed below.

4.2 Handling Missing Data

In general, Level 2A observations will not be produced at those locations that have no data or have erroneous data. As stated earlier, temperatures of 0 K and 320 K respectively will be used to denote these cases. For each of the locations at which a resampled Level 2A observation is produced, a negative temperature will be used to indicate that some of the requisite actual measurements were missing. When data gaps occur, a single value of Level 1A data might be produced through interpolation in order to permit construction of Level 2A data. This would only occur under very restricted circumstances, (circumstances that have not yet been specified). One necessary condition for such interpolation is that the resampling weight attached to the interpolated observation is below an unspecified threshold.

4.3 Correlations of Level 2A errors

As a result of the spatial averaging that produces the Level 2A data, errors of neighboring observations within any single channel will be somewhat correlated, (in contrast to the measurement errors of lower level data products that are assumed to be mutually independent). Errors between channels are not correlated in any case. Thus, while the Level 2A data set is well suited for applications that require combination of multiple channels of observations, the user should recognize that errors on observations within a single channel are not necessarily independent.

4.4 Numerical Computation Considerations

Computation of the weighting coefficients entails inversion of large matrices, an operation that can produce unstable results. This problem is alleviated with the addition

of even a small amount of smoothing. Because all of the weighting coefficients are computed using at least a small amount of smoothing, and the weighting coefficients are computed and tested long in advance of their application, there is no danger that numerical instability will affect the resampled data set.

5. References

Claassen, J.P., and A.K. Fung, The Recovery of Polarized Apparent Temperature Distributions of Flat Scenes from Antenna Temperature Measurements, *IEEE Transactions on Antennas and Propagation*, *AP-22* (3), 433-442, 1974.

Farrar, M.R., and E.A. Smith, Spatial Resolution Enhancement of Terrestrial Features Using Deconvolved SSM/I Microwave Brightness Temperatures, *IEEE Transactions in Geoscience and Remote Sensing*, *30* (2), 349--355, 1992.

Farrar, M.R., E.A. Smith, and X. Xiang, The Impact of Spatial Resolution Enhancement of SSM/I Microwave Brightness Temperatures on Rainfall Retrieval Algorithms, *Journal of Applied Meteorology*, *33*, 313-333, 1994.

Poe, G.A., Optimum Interpolation of Imaging Microwave Radiometer Data, *IEEE Transactions in Geoscience and Remote Sensing*, *28* (5), 800-810, 1990.

Robinson, W.D., C. Kummerow, and W.S. Olson, A Technique for Enhancing and Matching the Resolution of Microwave Measurements from the SSM/I Instrument, *IEEE Transactions in Geoscience and Remote Sensing*, *30* (3), 419--429, 1992.

Stogryn, A., Estimates of Brightness Temperatures from Scanning Radiometer Data, *IEEE Transactions on Antennas and Propagation*, *AP-26* (5), 720-726, 1978.